Energy barriers for point-defect reactions in 3*C*-SiC

Ming-Jie Zheng,[1] Narasimhan Swaminathan,[1,3] Dane Morgan,[1,2,*] and Izabela Szlufarska[1,2,†]
[1]*Materials Science and Engineering Department, University of Wisconsin-Madison, Madison, Wisconsin, USA*
[2]*Material Science Program, University of Wisconsin-Madison, Madison, Wisconsin, USA*
[3]*Department of Mechanical Engineering, Indian Institute of Technology Madras, Chennai 600036, India*
(Received 19 March 2013; revised manuscript received 5 July 2013; published 12 August 2013)

Energy barriers of the key annealing reactions of neutral and charged point defects in SiC are calculated with *ab initio* density functional theory methods. In order to effectively search for the lowest energy migration paths the preliminary path is first established based on *ab initio* molecular dynamics (AIMD) simulations. The energy barrier of each hop is then calculated via climbing image nudged elastic band methods for paths guided by the AIMD simulations. The final paths and barriers are determined by comparing different pathways. The annealing reactions have important implications in understanding the amorphization, recovery, and other aspects of the radiation response of SiC. The results are compared with the literature data and experimental results on SiC recovery and amorphization. We propose that the C interstitial and Si antisite annealing reaction may provide a critical barrier that governs both the recovery stage III and amorphization processes.

DOI: 10.1103/PhysRevB.88.054105 PACS number(s): 28.52.Fa, 61.72.Cc, 61.80.−x, 82.20.Wt

I. INTRODUCTION

Silicon carbide (SiC), due to its high temperature stability and low neutron-capture cross sections, is a promising candidate for structural and cladding applications in next-generation nuclear reactors.[1–3] Currently, SiC is being used to reduce fission-product release from the tristructural-isotropic (TRISO) fuel particles,[4] which are used in high-temperature gas-cooled reactors. 3*C*-SiC is the most widely explored SiC polytype for structural applications in nuclear reactors.[5] The response of SiC to radiation has therefore been studied extensively. One of the most dramatic responses of SiC to irradiation is its tendency to undergo radiation-induced amorphization (RIA). The amorphous phase has a lower mechanical strength,[6] and amorphization transition is also accompanied by swelling.[7] The accumulation of point defects is believed to be one of the main contributions to RIA of SiC and likely the dominant driving force for RIA during electron irradiation.[2,8–11] However, due to the complexity of defect energy landscape (EL) in SiC, the detailed mechanisms for RIA are still a subject of a debate. In this work, we aim to understand the mechanisms by which point defects can annihilate and therefore heal the radiation damage and at what temperature these mechanisms are active.

RIA in SiC, especially under electron irradiation, is believed to occur when the accumulation of point defects exceeds the critical level of damage.[10] The rate of damage accumulation is a result of the competition between the production and annihilation of point defects. A variety of point defects are produced in a short time (<ps) of a radiation cascade, including C interstitial (C_i), C vacancy (V_C), Si interstitial (Si_i), Si vacancy (V_{Si}), C antisite (C_{Si}), and Si antisite (Si_C). Thermal annealing enables interactions among point defects, and the interaction between pairs of defects in different recombination reactions is generally invoked as the primary method of defect reduction (in addition to interaction with sinks like grain boundaries and surfaces). Considering that the mobility of interstitials is much higher than that of vacancies, our work will focus on the interstitial-involved reactions in which no vacancy diffusion is required, such as the recombination reactions between interstitials and vacancies and the kick-out reactions between interstitials and antisites. For the recombination reactions, the homogeneous reactions among conjugate defects of the same sublattice (e.g., $C_i + V_C \rightarrow C_C$) can heal the material of damage and have been proposed to be the key processes governing the rapidly increasing dose to amorphization with temperature.[12] Heterogeneous recombination reactions (e.g., $C_i + V_{Si} \rightarrow C_{Si}$) between defects from unlike sublattices result in the formation of antisite defects, which result in some measure of healing but not completely. The kick-out reactions (e.g., $C_i + Si_C \rightarrow C_C + Si_i$) can only partially heal the damage by removing antisites, which reduces the chemical disorder of the material and hinders the amorphization in SiC. This kind of kick-out reaction can alter certain features of the dose to amorphization vs temperature curves[12] Since the homogeneous recombination reactions and kick-out reactions are critical in healing radiation damage in SiC, we focus our study on these processes.

The annealing properties of irradiated SiC have been studied by various experimental techniques, including photoluminescence (PL) spectroscopy,[13] optically detected magnetic resonance,[14] deep level transient spectroscopy (DLTS),[15,16] positron annihilation spectroscopy,[15,17] electron spin resonance (ESR),[17,18] and Rutherford backscattering spectrometry (RBS) together with the isochronal annealing.[2,19] The sharp reduction of D_2 (a second set of lines between 2.25 and 2.10 eV) PL intensity after 1600 °C indicated a possible high-temperature lattice recovery in as-grown and ion-implanted 3*C*-SiC, but the specific defects and recovery mechanism are not established.[13] DLTS and resistivity measurements in 3*C*-SiC showed that 90% of defects in neutron-irradiated SiC can be removed by annealing at 350 °C.[16] Through DLTS in 4*H*-SiC (*n*-type[20] or *p*-type[21]) and 6*H*-SiC (*n*-type[15]), multiple annealing stages were observed.[20] Three annealing stages were discovered by ESR.[17,18] The annealing kinetics were investigated by RBS together with isochronal annealing analysis, and the corresponding activation energies were estimated.[2,19] Each annealing stage corresponds to a significant decreasing of disorder at a certain range of annealing temperature.

TABLE I. Summary of the activation energies (E_a), temperature ranges and mechanisms of three recovery stages in 3C-SiC, 4H-SiC, and 6H-SiC. The abbreviations are as follows: T_{cr} is the critical temperature to amorphization; recom. is recombination; mig. is migration; int. is interstitials; vac. is vacancies; anti. is antisites; FP is Frenkel pairs. Close FP has separation between the interstitial and the vacancy $d_{FP} < 0.7a_0$, where a_0 is the lattice parameter of a unit cell.

Polytype of SiC		Stage I	Stage II	Stage III
3C-SiC	E_a (eV)	0.23 ∼ 0.38 (Ref. 22), 0.49 (Ref. 16)	0.74 ± 0.05 (Ref. 23), 0.9 (Ref. 22)	1.34 or 1.6 (Ref. 22), 1.5 ± 0.1 (Ref. 25), 1.53 (Ref. 23), 2.2 ± 0.3 (Ref. 18), 2.32 (Ref. 24), 2.35 (Ref. 23)
T_{cr} ∼ 340 K (Ref. 11)	Temperature (K)	170 ∼ 300 (Ref. 22), 300 (Ref. 16)	450 (Ref. 23), 570 (Ref. 16), 620 (Ref. 18)	650 (Ref. 23), 1020 (Ref. 18)
2-MV electron irradiation	Mechanism	close C-FP recomb.[22]	mig. of C_i (Ref. 23), close Si-FP recomb. (Ref. 22), $V_{Si} \rightarrow C_i + C_{Si}$ (Ref. 24)	C-FP recomb. (Ref. 22), mig. of Si_i (Refs. 23 and 25), mig. of V_{Si} (Ref. 23), $V_{Si} \rightarrow V_C + C_{Si}$ (Ref. 24)
6H-SiC	E_a (eV)	0.25 ± 0.1 (Ref. 19), 0.3 ± 0.15 (Ref. 2)	0.7 ± 0.2 (Ref. 32), 1.3 ± 0.25 (Ref. 2)	1.3 ± 0.2 (Ref. 32), 1.5 ± 0.3 (Refs. 2 and 19)
T_{cr} ∼ 501 ± 10 K (Ref. 31)	Temperature (K)	150 ∼ 300 (Ref. 2)	250 (Ref. 31), 450 ∼ 550(Ref. 2)	450 (Ref. 31), 570 ∼ 720 (Ref. 2)
2-MeV Au^{2+} ion irradiation	Mechanism	FP recomb. (Ref. 22)	mig. of int. and close FP recomb. (Ref. 31)	mig. of int. and close FP recomb. (Ref. 31), mig. of Si_i (Ref. 22) or V_{Si} (Ref. 14)
4H-SiC	E_a (eV)	N/A	0.89 ± 0.02 (Ref. 32)	N/A
T_{cr} ∼ 450 K (Ref. 32)	Temperature (K)	250 ∼ 420 (Ref. 32)	470 ∼ 570 (Ref. 32)	600 ∼ 700 (Ref. 32)
1.1 MeV Al_2^+ molecular ion irradiation	Mechanism	FP recomb.[32]	mig. of int. (Ref. 32)	mig. of vac. (Ref. 32)

The present knowledge of barriers and proposed mechanisms for the recovery stages in 3C-SiC, 6H-SiC, and 4H-SiC are summarized in Table I. In each polytype of SiC, there are three recovery stages, which are similar on both C and Si sublattices.[2] Here we take 3C-SiC as an example to summarize the recovery mechanisms reported in literature. Stage I (0.2 eV $< E_a <$ 0.5 eV) has been attributed to the recombination of close C or Si Frenkel pairs (FP),[22] in which the distance between interstitial and vacancy is small ($d_{FP} < 0.7a_0$, where a_0 is the lattice parameter of a unit cell). Stage II (0.7 eV $< E_a <$ 0.9 eV) has been associated with the migration of C_i,[23] close Si FP recombination,[22] or reaction $V_{Si} + C_i \rightarrow C_{Si}$.[24] Stage III (1.3 eV $< E_a <$ 2.4 eV) has been related to the C-FP recombination,[22] migration of Si_i[23,25] or V_{Si},[23] or the transformation from V_{Si} to a carbon vacancy and carbon antisite complex (V_C-C_{Si}).[24] These interpretations are not conclusive for at least two reasons. First, for stages II and III, the proposed mechanisms are different in different references, so it is clear that there is no consensus on the mechanisms. Second, the recovery stages were associated not with annealing reaction barriers but with migration barriers of defects. The migration energies of 0.74 eV for C_i, 1.53 eV for Si_i, 4.10 eV for V_C, and 2.35 eV for V_{Si} used in Refs. 23 and 25 do not match well with the recent *ab initio* migration barriers of 0.50 eV for C_i, 0.83 eV for Si_i, 3.66 eV for V_C, and 2.70 eV for V_{Si} from Refs. 26 and 27. Unlike metals where migration barriers govern the recombination reactions, recombination barriers in SiC can be greater than the migration barrier, and these high barriers can have profound implications on the amorphization response.[12] If no additional barrier is considered, the critical temperature to amorphization is too low, as predicted using the no-barrier model in Ref. 12. Due to the importance of defect reactions in governing the long-term microstructural evolution of the material, we need to consider the annealing reactions between point defects, such as recombination and kick-out reactions, and determine which reaction or reactions play a critical role in each recovery stage.

In addition to qualitative interpretations of damage recovery, the energy barriers of point-defect reactions are important input parameters for defect evolution models, which are capable of simulating amorphization or other long-term evolution of point defects in the material. These models are typically either rate theory models[10,12] or kinetic Monte Carlo simulations[28] parameterized with thermodynamic and kinetic data. However, the present understanding of recombination kinetics in SiC is not complete for such models to be accurate. Considering the homogeneous recombination reactions ($C_i + V_C \rightarrow C_C$ and $Si_i + V_{Si} \rightarrow Si_{Si}$), multiple studies have been done, but the values obtained for the corresponding recombination barriers are different. For example, the recombination barriers (E_r) for Si FP (Si_i and V_{Si}) were calculated as 0.03 eV in Ref. 29, 0.2 eV in Ref. 30, and 1.03 eV in Ref. 31. For the recombination of C FP (C_i and V_C), computational and experimental works have reported possible values for the barriers, but they all differ substantially. For example, the values of E_r determined using computational method were 0.4 eV in Ref. 30, 1.35 eV in Ref. 29, and 1.47 eV in Ref. 31; the values from experiments were 0.3 eV in Ref. 2, 0.7 eV in Ref. 32, and 0.9 eV in Ref. 33. Not only are the values of the barriers varying substantially amongst the various authors, but the fundamental features of ELs for the reactions were also different. Swaminathan *et al.*[12] have identified three categories of ELs based on the values of the recombination barrier (E_r), the trapping barrier (E_t), and the migration barrier (E_m). For C-FP recombination, Bockstedte *et al.*[30] gave a migration EL ($E_r \leqslant E_m$, $E_t \leqslant E_m$), and this suggested that E_m of C_i set the upper-limit barrier of the recombination of C_i and V_C. We note that the migration EL is equivalent to a diffusion-limited reaction, but we refer to it as a migration EL to be consistent with the notation from Swaminathan *et al.*[12] Lucas *et al.*[31] suggested a recombination EL ($E_r > E_t \approx E_m$). Roma *et al.*[29] reported a more complicated trapping EL ($E_r > E_m$, $E_t > E_m$) with the C_i being trapped near the V_C forming a C_i-V_C complex. One possible reason why the calculated recombination barriers and the ELs are so different between studies is that the ELs have many local minima and the final results can be quite sensitive to the initial path chosen for calculations. The choice of the initial path poses a significant challenge especially in multicomponent systems. The interaction between point defects can distort the EL severely over many neighbors distance between the defects and makes it difficult to guess the path *a priori*. Thus, we are motivated to choose a better initial choice of minimum energy path for the minimum energy paths and then determine the energy barriers.

In this work, we use *ab initio* methods to study the key annealing point-defect reactions in SiC by carefully establishing the paths for the reactions based on a series of simulations. Specifically, we use *ab initio* molecular dynamics (AIMD) simulation to first determine the path taken by one of the defects participating in the reaction. This path is then used to guide *ab initio* reaction barrier calculations via the climbing image-nudged elastic band (CI-NEB) method.[34] The initial CI-NEB calculations are made much shorter by breaking the hop into segments, with start/end points at apparent local minima of the initial path. To support that the CI-NEB results found the correct path, we also use the drag method,[29] which is able to include many images and has been used to study GaAs[35] and SiC[27,29] for cases where it was hard to obtain converged results from the NEB method. In general, the drag method is not expected to be more accurate than CI-NEB results, but it can be useful to identify cases where limited images or other problems may cause the drag method to converge to an inaccurate barrier. Using the above approaches, we study the $C_i + V_C$ and $Si_i + V_{Si}$ recombination and $C_i + Si_C$ and $Si_i + C_{Si}$ kick-out reactions. These reactions cover the possible reactions between two basic point defects through which damage can heal completely or partially. The detailed procedure of finding the path and calculating the barriers are illustrated for each point defect reaction in Sec. IV. Finally, our *ab initio* results are compared with the previous computational and experimental data in Sec. V.

II. METHODS

Ab initio calculations were performed with the Vienna *Ab initio* Simulation Package (VASP)[36–39] in the framework of density functional theory (DFT) and the projector-augmented wave (PAW) method. The exchange-correlation was treated in the generalized gradient approximation (GGA), as parameterized by Perdew, Burke, and Ernzerhof.[40] The PAW potentials were generated with the following valence electronic configurations: $3s2\ 3p2$ for Si and $2s2\ 2p2$ for C. We also checked to what extent the choice of the exchange correlation function [GGA as opposed to the local density approximation (LDA) used in Ref. 30] influenced the results. The difference between recombination barriers obtained using GGA and LDA is smaller than 0.2 eV/defect, thus the choice of GGA vs LDA for the exchange correlation should not have a large influence on our results.[31]

We used $3 \times 3 \times 3$ cubic supercells of $3C$-SiC containing 216 atoms (217 atoms for kick-out reactions). The system-size convergence was checked by comparing the energy barriers in 64-atom cell with those in 216-atom cells. The energy barrier difference is within an acceptable error range of 1 meV/atom. We chose to use the larger 216-atom cell because our systems often include two defects. For our 216-atom (217-atom) cell, we used a $2 \times 2 \times 2$ K-point mesh, which had an error lower than 1 meV/atom when compared to a $3 \times 3 \times 3$ K-point mesh. An energy cut-off of 450 eV was used.

In order to find the minimum energy path effectively, we used AIMD simulation as a guide for our CI-NEB calculation. The two defects are located in the simulation cell such that one is the fourth (or sixth) nearest neighbor (NN) to the other. The NVT ensemble was then used to simulate the time evolution of the defected system at a temperature of 2000 K, which is below the melting temperature of SiC ($\sim$3123 K) and is just high enough to observe the recombination/kick-out path. AIMD at these high temperatures may take paths that are not relevant at lower temperatures, which is a limitation of using such high temperatures. However, these temperatures are necessary to see recombination events on practical time scales for investigating many paths. In practice, these high-temperature AIMD searches did yield novel low-energy paths for lower temperature migration. A time step of 3 fs was used, and we simulated each ensemble for about 6 ps. While this time step is too large for accurate long-time MD simulations,

it is a reasonable compromise between time and accuracy for relatively short simulations focused on identifying the reaction path. Repeating several MD runs with a smaller 1-fs time step yielded similar reaction paths as those used with a 3-fs time step, demonstrating that this longer time step is generally adequate for the path identification. The path from AIMD contained some apparently intermediate stable positions, which were used to divide the path into subpaths. The energy barrier of each subpath was calculated via the CI-NEB method (typically with one or three images), which used the initial state, intermediate stable states, and the final state as endpoints. We also checked the possible bias effect of forcing these intermediate stable states as endpoints by removing them one by one and found that any bias effect is negligible. The drag method, which was used to check the CI-NEB results, drags the moving atom(s) from initial to final state. One coordinate of the moving atom was fixed. An anchor atom that was far from the moving atom was also totally fixed to prevent the shift motion of the whole system. Other atoms in the system were relaxed freely.

At finite temperatures, the critical quantity governing the defect formation and diffusion is the Gibbs free energy.[41] Since changes in pressure P and volume V are negligibly small in most cases,[41] the free energy for defect formation[27] and migration can be written in terms of the Helmholtz energy

$$F_{f/m} = U_{f/m} - TS_{f/m}, \tag{1}$$

where $U_{f/m}$ represents the finite-temperature formation or migration energy, respectively, and $S_{f/m}$ is the formation or migration entropy, respectively. As mentioned in Ref. 27, the formation energy E_f alone has been used for semiquantitative prediction of the equilibrium-defect concentrations to within a few orders of magnitude. Furthermore, since we are not predicting defect concentrations, we will not consider the finite-temperature contributions to formation free energies here. However, we will briefly discuss the possible impacts of finite-temperature effects on the migration free energies. Since changes in U_m are typically governed by the equipartition theorem, they tend to cancel in the energy differences used to calculate migration and can therefore be ignored. The dominant finite-temperature effects are therefore likely to be from S_m. In Ref. 41, the entropy contribution to the free energy of activation for vacancy migration was 0.3 eV at 1800 K in 3C-SiC, which corresponds to about $2k_B$. Assuming this value is typical for S_m, in the temperature range we are interested in (700 K or below), the scale of the entropy contribution to F_m is around $0.1 \sim 0.2$ eV. These values are small enough to ignore and still allow semiquantitative determination of reaction barriers for understanding amorphization and damage recovery. We therefore will make the assumption that $E_m \approx F_m$, where E_m is the zero-temperature migration energy without vibrational contributions, and use E_m for all our migration energies. However, at higher temperatures, the neglected terms in the free energy are likely to be significant,[27] and the present values must be applied only qualitatively. More complete calculations, including the vibrational degrees of freedom, should be pursued in future studies.

The defect-formation energy E_f is given by[26]

$$E_f = E_{\text{def}} - E_{\text{perfect}} + \sum_i \Delta n_i \mu_i + q\big[E_{VBM} + \mu_F + \left(E^{\text{core}}_{\text{def}} - E^{\text{core}}_{\text{perfect}}\right)\big] + E_{MP}, \tag{2}$$

where E_{def} is the energy of the defected cell, E_{perfect} is the energy of the perfect cell, Δn_i is the change in the number of species i (i = Si or C) when the defect forms, and μ_i is the chemical potential of species i. We set $\mu_i = \mu_i^0$ for species i-rich condition, otherwise $\mu_i = \mu_i^0 + \Delta E_{\text{SiC}}$, where μ_i^0 is the chemical potential of species i in the stable, pure bulk single-crystal phase (diamond structure for Si and graphite for C) and $\Delta E_{\text{SiC}} = \mu^0_{\text{SiC}} - \mu_i^0 - \mu^0_{\text{Si}} - \mu^0_{\text{C}}$. q is the number of net electrons in the supercell. E_{VBM} is the energy of the valence band maximum in the perfect cell. The term $E_{VBM} + \mu_F + (E^{\text{core}}_{\text{def}} - E^{\text{core}}_{\text{perfect}})$ is the chemical potential of the electron, μ_F is the Fermi level relative to E_{VBM}. $E^{\text{core}}_{\text{def}} - E^{\text{core}}_{\text{perfect}}$ is an electronic potential shift, where $E^{\text{core}}_{\text{def}}$ and $E^{\text{core}}_{\text{perfect}}$ represent the corelike electronic levels in the defected cell and prefect cell, respectively. $E_{MP} = -\frac{q^2\alpha}{2\varepsilon L} - \frac{2\pi q Q}{3\varepsilon L^3}$ is the correction for the electrostatic energy proposed by Makov and Payne[42] and followed by Leslie and Gillan,[43] where α is the lattice-dependent Madelung constant, L is the length of the supercell, Q is the quadrupole moment, and ε is the dielectric constant.

In this work, we consider the Fermi level (μ_F) of SiC ranging from midgap to the conduction band minimum (the latter corresponding to a strongly n-type material), because the as-prepared SiC is generally n-type,[44–47] and μ_F of irradiated SiC is often considered to be pinned by defect levels around midgap.[48] However, due to the band-gap prediction errors in the DFT calculations [the band gap, E_g, in 3C-SiC is about 1.20 (1.40) eV from LDA[27] (GGA) as compared to the experimental value of 2.37 eV[49]], it is difficult to obtain from our calculations or the literature[27,30] the correct stable charge states for even isolated SiC defects with μ_F at midgap and conduction band minimum. Furthermore, in this study, defect pairs must be considered, and the charge states of these defect pairs have generally not been explored previously. Among different methods proposed to solve the band-gap problem, a scaling approach by the use of a scissor operator[50] is a practical approach to treat our complicated system with defect pairs. While this scaling approach is a significant and poorly controlled approximation,[51] it is used here only for a few defects and only to determine qualitatively the relevant charge states over a range of μ_F, not to determine precise defect-level positions.

III. STABLE CHARGE STATES, DEFECT PAIR STRUCTURES, AND ENERGIES

The stable charge states for isolated point defects and defect pairs when μ_F is at the midgap and the conduction band minimum are summarized in Table II. The Green function-screened Coulomb interaction (GW),[24,52] or hybrid results,[53] are used when they are available, and GW is preferred when there is any inconsistency. We compared these stable charge states with our results from the scaling approach and found that 9 of 10 results agree very well, and the only exemption is V_C

TABLE II. Stable charge states and corresponding formation energies (E_f) of four defect reactions and related point defects with μ_F at midgap or conduction band minimum (n-type) in SiC. A description of the nearest neighbor (NN) positions can be found in Sec. III.

	Charge states for different μ_F			
	Midgap		Conduction band minimum	
Defect reactions	Charge	E_f (C-rich) (eV)	Charge	E_f (C-rich) (eV)
$C_{sp\langle 100\rangle} + V_C \rightarrow C_C$				
$C_{sp\langle 100\rangle}$	2+	8.79	0	6.45
V_C	2+	6.10	0	4.72
$C_{sp\langle 100\rangle} + V_C$ (4thNN)	4+	14.79	0	10.57
$Si_{sp\langle 110\rangle} + V_{Si} \rightarrow Si_{Si}$				
$Si_{sp\langle 110\rangle}$	2+	11.91	0	9.00
V_{Si}	1−	5.94	2−	4.52
$Si_{sp\langle 110\rangle} + V_{Si}$ (6thNN)	0	16.07	2−	13.39
$Si_{TC} + V_{Si} \rightarrow Si_{Si}$				
Si_{TC}	4+	11.97	0	8.98
V_{Si}	1−	5.94	2−	4.52
$Si_{TC} + V_{Si}$ (9thNN)	3+	17.98	2−	13.18
$C_{sp\langle 100\rangle} + Si_C \rightarrow C_C + Si_i$				
$C_{sp\langle 100\rangle}$	2+	8.79	0	6.45
Si_C	0	4.36	0	4.36
$C_{sp\langle 100\rangle} + Si_C$ (4thNN)	2+	13.09	0	10.74
$Si_{sp\langle 110\rangle} + C_{Si} \rightarrow Si_{Si} + C_i$				
$Si_{sp\langle 110\rangle}$	2+	11.91	0	9.00
C_{Si}	0	3.48	0	3.48
$Si_{sp\langle 110\rangle} + C_{Si}$ (4thNN)	2+	14.83	0	12.03

at the conduction band minimum (0 from GW, 2+ from the scaling approach). Considering such good performance of the scaling approach in SiC and the computationally expensive cost of GW and hybrid, for cases where no hybrid or GW studies are available, which include all antisites (C_{Si} and Si_C) and defect pairs, we calculated charge states using the scaling approach. As shown in Table II, except for the neutral Si FP $Si_{sp\langle 110\rangle} + V_{Si}$ with μ_F at midgap, all of the stable charges of defect pairs are equal to the summation of charges of isolated defects for both midgap and n-type SiC. This general consistency suggests that the defect interactions do not change the defect-charge states in most cases. Table II also shows the formation energies (at C-rich condition) of point defects and defect pairs involved in key reactions at the stable charge state for the corresponding μ_F. The definition of formation energies will be described in detail in the next section.

While describing the path that the defects take to recombine, it is important to illustrate the relative position of the mobile defect atom in the simulation cell. To accomplish this, we extracted a region from the supercell containing the defects and described the positions of the interstitial atom in terms of the neighbor distance ranging from the first NN (1stNN) to the sixth NN (6thNN) with the vacancies (V_C, V_{Si}) or the antisites (Si_C and C_{Si}) as the origin (0thNN). Neighbors are counted independent of the sublattice, so for perfect SiC, the 1stNN are all of opposite type of the original atom. An example of the path that used stable configurations of C FP is shown in Fig. 1. The relative positions of C_i at 1stNN to 6thNN are marked by numbers 1 to 6. Among these configurations, the interstitial structures are C-Si dumbbells (C_{spSi}) in both 1stNN and 5thNN and C-C dumbbells (C_{sp}) for other configurations. The orientations of dumbbells for these configurations are denoted as (1) $C_{spSi\langle 010\rangle tilted}$, (2) $C_{sp\langle 010\rangle tilted}$, (3) $C_{sp\langle 001\rangle tilted}$, (4) $C_{sp\langle 001\rangle tilted}$, (5) $C_{spSi\langle 010\rangle tilted}$, and (6) $C_{sp\langle 100\rangle tilted}$. $C_{spSi\langle 010\rangle tilted}$ means a C-Si split dumbbell at the Si site along the tilted $\langle 010\rangle$ direction, $C_{sp\langle 010\rangle tilted}$ means a C-C split dumbbell at the C site along the tilted $\langle 010\rangle$ direction, and the other cases are defined analogously.

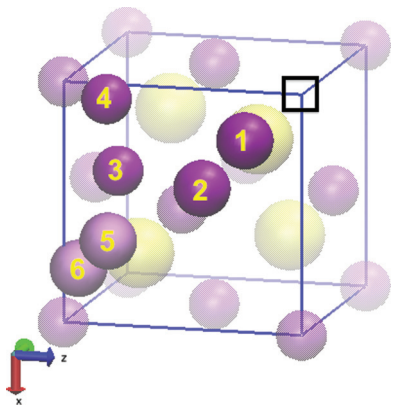

FIG. 1. (Color online) Configurations of stable C-Frenkel pairs with relative positions of C_i at (1) 1stNN, (2) 2ndNN, (3) 3rdNN, (4) 4thNN, (5) 5thNN, and (6) 6thNN. The square marks the C vacancy site. The interstitial atoms in 1stNN to 4thNN are represented with dark purple balls (C166), and 5thNN to 6thNN are represented with light pink balls (C122). The fcc structure formed by C atoms (transparent purple balls) are extracted from a 216-atom cell. The Si atoms included in the fcc box are shown by the transparent yellow balls.

TABLE III. Formation energies (E_f) at C-rich condition, binding energies (E_b), and separation (d_{def}) of the neutral and charged defect pairs (see detailed description in the text). A description of the nearest neighbor (NN) positions can be found in Sec. III.

Configuration	Charge	E_f (C-rich) (eV)	E_b (C-rich) (eV)	d_{def} (a_0)
$C_{sp\langle 100\rangle} + V_C$	0 (n-type)			
0thNN		0.00	−11.17	0.00
1stNN		5.88	−5.29	0.30
2ndNN		9.48	−1.69	0.57
3rdNN		10.89	−0.26	0.84
4thNN		10.57	−0.6	0.81
5thNN		11.61	0.46	1.05
6thNN		10.32	−0.83	1.29
$C_{sp\langle 100\rangle} + V_C$	4+ (mid-gap)			
0thNN		9.96	−4.85	0.00
4thNN		14.61	−0.02	0.86
$Si_{sp\langle 110\rangle} + V_{Si}$	0 (mid-gap)			
6thNN		16.07	−0.52	1.16
$Si_{sp\langle 110\rangle} + V_{Si}$	2− (n-type)			
0thNN		−1.37	−14.9	0.00
6thNN		13.39	−0.13	1.16
$Si_{TC} + V_{Si}$	3+ (midgap)			
0thNN		7.29	−10.62	0.00
3rdNN		17.65	−0.26	0.87
9thNN		17.98	0.07	1.50
$Si_{TC} + V_{Si}$	2− (n-type)			
9thNN		13.18	−0.33	1.50
$C_{sp\langle 100\rangle} + Si_C$	0 (n-type)			
0thNN		9.01	−1.8	0.00
1stNN		9.68	−1.13	0.43
4thNN		10.74	−0.07	0.80
6thNN		10.82	0.01	1.42
$C_{sp\langle 100\rangle} + Si_C$	2+ (midgap)			
0thNN		11.92	−1.23	0.00
1stNN		12.30	−0.84	0.42
4thNN		13.09	−0.05	0.85
$Si_{sp\langle 110\rangle} + C_{Si}$	0 (n-type)			
0thNN		6.45	−5.25	0.00
2ndNN		12.33	0.63	0.62
4thNN		12.03	0.33	0.85
$Si_{sp\langle 110\rangle} + C_{Si}$	2+ (midgap)			
0thNN		8.73	−6.64	0.00
4thNN		14.83	−0.54	0.85

The interaction between defects is measured by the binding energy (E_b) of the defect pair, which is defined as the difference between E_f of the defect pair and the sum of E_f of the isolated defects. For example, for a C FP, we define E_b(C FP) = E_f(C FP) − [E_f(C_i) + E_f(V_C)], where $E_f(X)$ is the formation energy of the X defect. Note that $E_b < 0$ means the defects are attracted to each other. We define d_{def} (in units of DFT lattice parameter $a_0 \approx 4.37$ Å) to represent the separation between two defects in a pair, e.g., the distance between C_i and V_C in the C FP. The E_f, E_b, and d_{def} of neutral and charged defect pairs are shown in Table III. The corresponding μ_F (midgap or conduction band minimum) at which the charge state is stable is marked in the parentheses. We choose the relatively well-separated defect pairs 4thNN or 6thNN as the starting point for the recombination paths. Most of the starting points have relatively small binding energies $|E_b| < 0.6$ eV, except the 6thNN of $C_{sp\langle 100\rangle} + V_C$ ($E_b \approx -0.83$ eV), which has a quite high absolute value and may be of interest for future study. Thus, we assume that separations of most starting points are far enough apart and the migration barriers to farther neighbors are unlikely to differ significantly from bulk values.

IV. ENERGY BARRIERS

We summarize energy barriers of important hops in Table IV. The barriers (forward/backward) are calculated using GGA in a 216-atom supercell for recombination and in a 217-atom supercell for kick-out reactions. Several LDA results are also listed to help illustrate LDA vs GGA differences, which are within a range of 0.01 ∼ 0.27 eV. This indicates that LDA and GGA results for migration energies are comparable to each other. The corresponding literature data are also listed for comparison. We now explain the determination of the paths and energy barriers for these four reactions in detail. Note that

TABLE IV. Energy barriers of the four key point-defect reactions in SiC. Numbers 0 to 6 stand for the 0th to 6th nearest neighbors (NNs). Energies formatted as A/B refer to a forward reaction energy A and a reverse reaction energy B.

Reaction Hop	This work 216 atoms GGA	216 atoms LDA	Ref. 28 216 atoms LDA	Ref. 30 64 atoms GGA	Ref. 29 64 atoms LDA	Ref. 55 72 atoms LDA
$C_{sp\langle 100\rangle} + V_C \rightarrow C_C$						
$6 \rightarrow 2$	1.51/2.21					
$6 \rightarrow 1$	1.48/5.72					
$6 \rightarrow 0$	1.47					
$4 \rightarrow 3$	1.05					
$4 \rightarrow 2$	0.90/1.97	0.69/1.70	1.35/2.00			
$4 \rightarrow 1$	0.86/5.55	0.72/5.54				
$4 \rightarrow 0$ (curved)	0.86	0.69				
$4 \rightarrow 0$ (4+, curved)	1.88					
$4 \rightarrow 0$ (linear)	1.48			1.43		
$2 \rightarrow 1$	0.43					
$2 \rightarrow 0$	0.43				0.4	
$2 \rightarrow 0$ (1+)	0.49				0.5	
$1 \rightarrow 0$	0.1	0.15	0.2			
$Si_{sp\langle 110\rangle} + V_{Si} \rightarrow Si_{Si}$						
$6 \rightarrow 0$	0.03		0.03		0.2	
$6 \rightarrow 0$ (2-)	0.17					
$6 \rightarrow 0$ (2+)	0				0	
$6 \rightarrow 3$	0					
$Si_{TC} + V_{Si} \rightarrow Si_{Si}$						
$9 \rightarrow 0$	1.76			1.84		
$9 \rightarrow 0$ (3+)	2.26					
$9 \rightarrow 0$ (2−)	1.85					
$3 \rightarrow 0$ (interstitial)	0.68					
$3 \rightarrow 0$ (interstitialcy)	2.26			2.37		
$C_i + Si_C \rightarrow C_C + Si_i$						
$6 \rightarrow 1$	0.60/1.75					
$4 \rightarrow 1$	0.61/1.67					
$1 \rightarrow 0$	1.34/2.02	1.33/2.23			2.00/3.00	NA/1.80
$1 \rightarrow 0$ (2+)	2.24					
$Si_i + C_{Si} \rightarrow Si_{Si} + C_i$						
$4 \rightarrow 0$	0.64/6.23	0.61/5.96				NA/5.90
$4 \rightarrow 0$ (2+)	0.35					

for each reaction, the analysis starts with the system in the neutral state (no charge added to the cell) and determines the fastest path for recombination for that neutral state. Then the possible charge states (as shown in Table II) that might occur for different μ_F (midgap or conduction band minimum) are considered. The initial path for each charge-state reaction is taken from the fastest path of the corresponding neutral calculation. This approach assumes that the fastest path does not change significantly when the charge state varies in response to different electron chemical potential.

A. Recombination reaction $C_i + V_C \rightarrow C_C$

The recombination of C FP is a very important annealing reaction in SiC because it provides a direct mechanism to reduce the concentration of C_i and V_C, which are the dominant defects produced under irradiation.[54] It is also prevalent at quite low temperatures, as the C_i atoms are the first defect type to become mobile with increasing temperature.[27] However, as discussed in the Introduction, the recombination barriers of C FP have a wide range of values in literature. To overcome this problem, we searched the minimum energy path of this recombination as follows.

For μ_F at the conduction band minimum, the stable charge states of C_i, V_C, and C FP are neutral, as shown in Table III. From the AIMD simulation with a starting point of neutral 4thNN, the C_i atom starts from position 4 ($C_{sp\langle 001\rangle tilted}$), passes the nearer positions 2 ($C_{sp\langle 010\rangle tilted}$) and 1 ($C_{spSi\langle 010\rangle tilted}$), and finally recombines with V_C at position 0. Thus the path suggested from AIMD is $4 \rightarrow 2 \rightarrow 1 \rightarrow 0$. Note that we will often refer to neighbors in paths with just their numbers (i.e., 4 instead of 4thNN) to avoid cumbersome repetition of the NN symbol. The four positions involved along this path correspond to the initial, two potentially intermediate, and final states for the recombination process. After full relaxation of the four configurations from AIMD, we obtained four stable states: 4thNN (initial state), 2ndNN (intermediate state), 1stNN (intermediate state), and 0thNN (final state).

Using the four fully relaxed configurations as endpoints for the CI-NEB calculation, we calculated the energy barriers

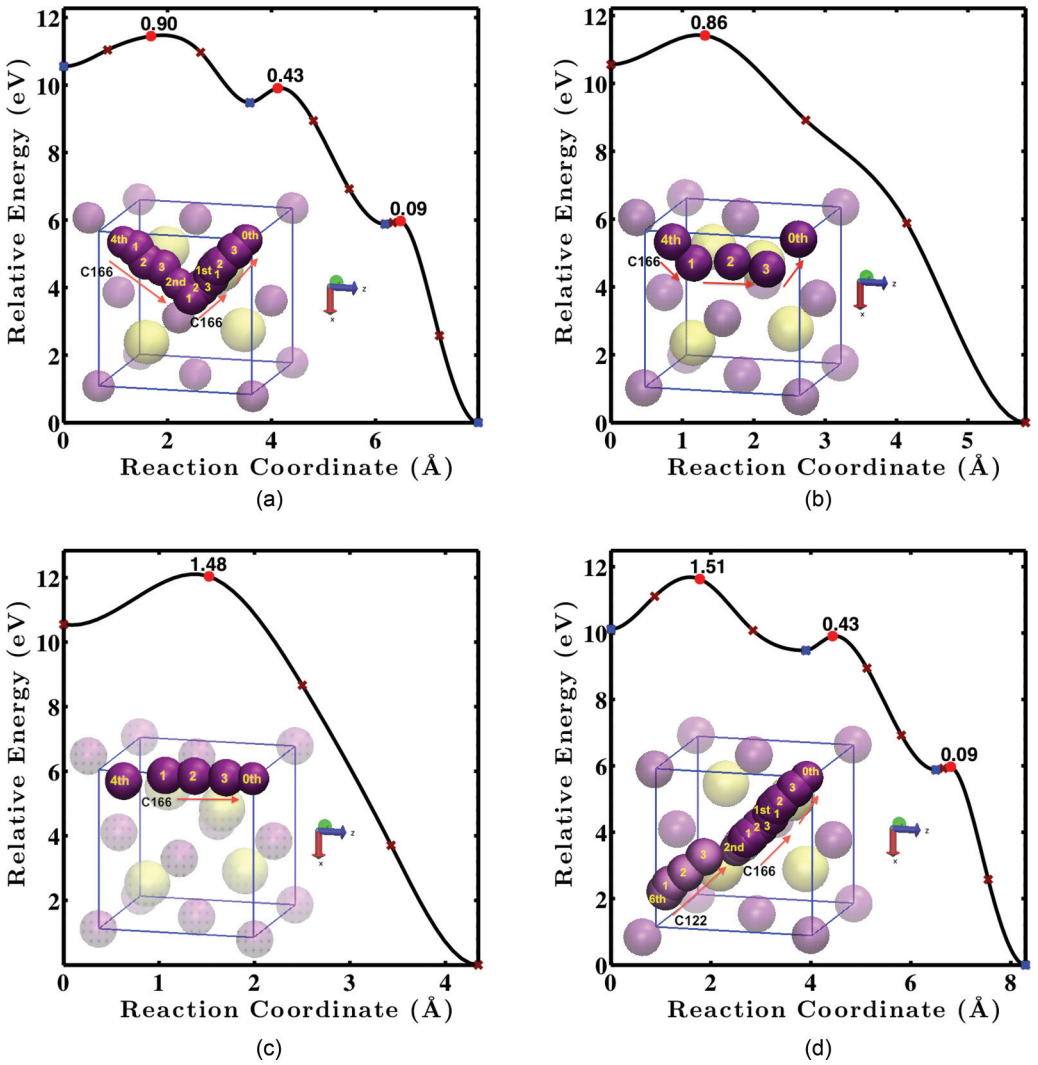

FIG. 2. (Color online) ELs of $C_i + V_C \rightarrow C_C$ along paths (a) $4 \rightarrow 2 \rightarrow 1 \rightarrow 0$, (b) $4 \rightarrow 0$ (curved), (c) $4 \rightarrow 0$ (straight), and (d) $6 \rightarrow 2 \rightarrow 1 \rightarrow 0$. The insets show the paths in CI-NEB; dark purple balls represent the C_i atoms in the endpoints and images of CI-NEB. The endpoints and image numbers are marked on the balls. The moving direction of C_i is shown by the red arrows. The light purple and yellow balls represent other C and Si atoms in the configuration, respectively. The solid lines show the ELs obtained from CI-NEB runs. The blue squares and brown crosses on ELs represent the relative energies of CI-NEB endpoints and images with respect to the energy of the final (right) endpoint, respectively. The red dots illustrate the local maxima image energies. The marked values are energy barriers relative to the energy of the initial (left) endpoint for each CI-NEB run. The atom species number label [C166 (dark purple balls) and C122 (pink balls)] refers to the atom numbering in the supercell used for the calculations.

for three hops along the $4 \rightarrow 2 \rightarrow 1 \rightarrow 0$ path, as shown in Fig. 2(a). Note that in Fig. 2, the C interstitial atom is C166 (or C122), where here and below the numbered atoms refer to the atom index in the supercell used in the calculations. The $4 \rightarrow 2$ hop has a barrier of 0.90 eV, $2 \rightarrow 1$ hop has a barrier of 0.43 eV, and $1 \rightarrow 0$ hop has a barrier of 0.09 eV, and thus the recombination barrier along this path is 0.90 eV. Since the use of the two intermediate states at 1stNN and 2ndNN as endpoints may bias the path, we refer to them as constraints and will remove them from the path step by step. We note that if the intermediates are in fact stable local minima along the path, then for fully converged CI-NEB calculations the use of (i) a series of CI-NEB calculations with these intermediates as endpoints, or (ii) a single unconstrained CI-NEB with many images that passes through the minima, will be identical. In this sense, the use of the intermediates does not really introduce any additional constraints and removing them should have no effect. However, due to computational limitations, the calculations here are done with few images, and convergence is a continual challenge. Therefore, it is not clear that the formally equivalent approaches (i) and (ii) are in fact numerically equivalent. Therefore, we will always use both approaches, viewing the intermediates as constraints whose removal might change the results due to numerical issues. Removing one endpoint at either the 1stNN or the 2ndNN, we got two similar paths: $4 \rightarrow 2 \rightarrow 0$ with a barrier of 0.90 eV and $4 \rightarrow 1 \rightarrow 0$ with a barrier of 0.86 eV. Since the $4 \rightarrow 1 \rightarrow 0$ path has a slightly lower barrier, we will use it as an example to explain the removal of constrained endpoints as follows. We combined the two separate CI-NEB calculations ($4 \rightarrow 1$, $1 \rightarrow 0$) into a

single CI-NEB calculation ($4 \rightarrow 0$). The latter CI-NEB images were taken as the peak of $4 \rightarrow 1$ hop, the endpoint 1stNN, and the peak of $1 \rightarrow 0$ hop from the former two separate runs. This allows the CI-NEB to optimize without forcing the path to pass through exactly point 1, as it is now an image rather than a fixed endpoint. The barrier along this less constrained path $4 \rightarrow 0$ [Fig. 2(b)] was calculated to be 0.86 eV. The barrier difference between $4 \rightarrow 0$ and $4 \rightarrow 2 \rightarrow 1 \rightarrow 0$ is about 0.04 eV, which is within the numerical error bar and shows both calculations yield essentially identical results. It is possible that the $4 \rightarrow 0$ calculation, with enough images and with guiding from AIMD, would find essentially the same pathway as $4 \rightarrow 2 \rightarrow 1 \rightarrow 0$. However, if the images for the $4 \rightarrow 0$ calculation are from linear interpolation, as shown in Fig. 2(c), the barrier is 1.48 eV, which is much higher than the previous barrier; it indicates that the straight path is not favorable.

We also considered a starting point of the 6thNN ($C_{sp\langle 100\rangle tilted}$) because, like the 4thNN, it is a second NN of the 2ndNN position (where the 2ndNN was used as above to refer specifically to the interstitial being a 2ndNN of the V_C). The path suggested from AIMD is $6 \rightarrow 2 \rightarrow 1 \rightarrow 0$, as shown in [Fig. 2(d)]. The barrier along this path calculated via CI-NEB is 1.51 eV, which is contributed from the $6 \rightarrow 2$ hop. The barrier is significantly higher than the recombination barrier along the $4 \rightarrow 2 \rightarrow 1 \rightarrow 0$ path (0.90 eV). Thus, there is no low barrier path directly from the 6thNN to recombine, and it is presumably preferred for the C_i atom to migrate from 6thNN to 4thNN with a barrier comparable to the migration barrier of $C_{sp\langle 100\rangle}$, and then along the $4 \rightarrow 2 \rightarrow 1 \rightarrow 0$ path to recombine with V_C. Therefore, the minimum energy path for recombination reaction $C_C + V_C \rightarrow C_C$ is the $4 \rightarrow 2 \rightarrow 1 \rightarrow 0$ path with recombination barrier (E_r) of 0.90 eV. For this C recombination, E_r is higher than the migration barrier of $C_{sp\langle 100\rangle}$ ($E_m \sim 0.60$ eV), and there is no trapping ($E_r > E_t \approx E_m$), so the EL along this path is a recombination profile.

To check the CI-NEB result, we also used the drag method[29] to calculate the recombination barriers of C recombination. The initial and final points were still the neutral 4thNN and 0thNN of C FP. Between the two endpoints 4 and 0, the C_i atom was dragged into 13 different positions along the $4 \rightarrow 2 \rightarrow 1 \rightarrow 0$ path. The z direction of the C_i atom was fixed in each configuration, while it could freely move on the x-y plane. An anchor atom that was $L/2$ from the C_i and V_C was fixed to avoid the rigid body motion of the entire computational cell. Other atoms were allowed to relax freely. After this constrained relaxation of each configuration, we obtained a barrier of 0.91 eV along the $4 \rightarrow 2 \rightarrow 1 \rightarrow 0$ path, which is only 0.01 eV larger than what was obtained using the CI-NEB method. We therefore predict that the neutral C FP recombines with a barrier of 0.90 eV, which is 0.30 eV higher than the migration barrier of 0.60 eV for $C_{sp\langle 100\rangle}$.

The neutral C FP is stable for SiC with μ_F at conduction band minimum, but when μ_F is at midgap, the stable charge state becomes $4+$, which consists of $C^{2+}_{sp\langle 100\rangle}$ and V_C^{2+}, as shown in Table II. The recombination path for C FP ($4+$) was found to be $4 \rightarrow 2 \rightarrow 0$ from AIMD simulation starting from the 4thNN ($4+$), and the barrier was calculated to be 1.88 eV by CI-NEB. This value is much higher than the recombination barrier of the neutral C FP and a little higher than the migration barrier of 1.40 eV for $C^{2+}_{sp\langle 100\rangle}$ (see Ref. 27). Therefore, the EL type of C FP ($4+$) recombination is also a recombination profile.

B. Recombination reaction $Si_i + V_{Si} \rightarrow Si_{Si}$

When μ_F is around the midgap, from Table II, the stable Si FP is the neutral $Si_{sp\langle 110\rangle} + V_{Si}$, where $Si_{sp\langle 110\rangle}$ is the $\langle 110\rangle$-oriented silicon split-interstitial. If $Si_{sp\langle 110\rangle}$ is at the 2ndNN or the 4thNN sites of V_{Si}, the configuration is not stable and will recombine immediately. A stable configuration of the FP $Si_{sp\langle 110\rangle} + V_{Si}$ can be obtained for the 6thNN (note that our 6thNN is similar to the 4thNN in Ref. 30). As orientation may play an important role in the Si FP $Si_{sp\langle 110\rangle} + V_{Si}$, we have chosen the orientation of the silicon-split interstitial to give the lowest energy for each case. As shown in Table II, the formation energy for the 6thNN [$Si_{sp\langle 110\rangle} + V_{Si}$ (0)] (16.07 eV) is much lower than that of the 9thNN [$Si_{TC} + V_{Si}$ ($3+$)] (18.08 eV). Thus the 6thNN [$Si_{sp\langle 110\rangle} + V_{Si}$ (0)] is more stable for midgap SiC. Due to the relative small binding energy of the 6thNN ($E_b \sim -0.52$ eV), the interaction between $Si_{sp\langle 110\rangle}$ and V_{Si} is relatively weak, and the landscape of interstitial hops for more distant neighbors is likely to be quite close to that of an isolated interstitial. Therefore, we consider the 6thNN as the starting point for our analysis of the recombination barrier of the Si FP $Si_{sp\langle 110\rangle} + V_{Si}$.

From AIMD simulation starting from the 6thNN, we can see that the recombination occurs following an interstitialcy mechanism: the Si interstitial atom (Si1) starts from the 6thNN site, then kicks out another Si atom (Si16) at the 2ndNN site, and the new Si interstitial atom (Si16) recombines with V_{Si}. This path from AIMD is denoted as $6 \rightarrow 2/2' \rightarrow 0$, where $2/2'$ means that the kicking out happens at the 2ndNN site.

The initial images for CI-NEB calculation were set up guided by the path from AIMD. The recombination barrier and EL for $Si_{sp\langle 110\rangle} + V_{Si}$ FP recombination along the path $6 \rightarrow 2/2' \rightarrow 0$ were obtained, as shown in Fig. 3(a). The CI-NEB path was very similar to the AIMD path, as described above. The CI-NEB barrier along this path $6 \rightarrow 2/2' \rightarrow 0$ is 0.03 eV, which was confirmed by the drag method and also matches with the results in Ref. 29. This 0.03 eV recombination barrier is much lower than the migration barrier of 0.80 eV for $Si_{sp\langle 110\rangle}$ based on our calculation, and no trapping is found, which indicates a migration EL. Thus, the recombination of FP $Si_{sp\langle 110\rangle} + V_{Si}$ along the path $6 \rightarrow 2/2' \rightarrow 0$ is limited by the migration of $Si_{sp\langle 110\rangle}$.

For μ_F at the conduction band minimum, there are two kinds of stable Si FP $Si_{sp\langle 110\rangle} + V_{Si}$ ($2-$) and $Si_{TC} + V_{Si}$ ($2-$), for both of which the charge $2-$ is from V_{Si}^{2-}. Their formation energies are similar to each other (13.39 eV and 13.18 eV for $Si_{sp\langle 110\rangle} + V_{Si}$ ($2-$) and $Si_{TC} + V_{Si}$ ($2-$), respectively), as shown in Table II. We focus initially on $Si_{sp\langle 110\rangle} + V_{Si}$ ($2-$) $\rightarrow$ Si_{Si} ($2-$), as the recombination path is similar to that in the neutral case described above, and the barrier of this charged defect recombination reaction is 0.17 eV. While this is somewhat higher than that for the uncharged defect, it is still very low, which is consistent with a migration type EL.

We also consider recombination from the $Si_{TC} + V_{Si}$ ($2-$) starting point, as it is actually the most stable Si FP structure when μ_F at conduction band minimum. For $Si_{TC} + V_{Si}$

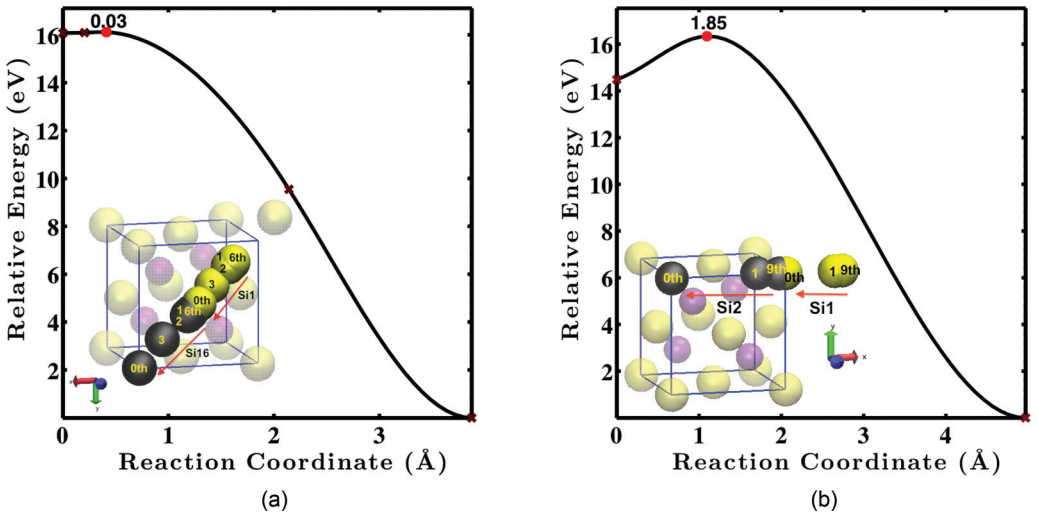

FIG. 3. (Color online) ELs of (a) $Si_{sp\langle 110\rangle} + V_{Si} \rightarrow Si_{Si}$ along the path $6 \rightarrow 2/2' \rightarrow 0$ and (b) $Si_{TC} + V_{Si}^{2-} \rightarrow Si_{Si}^{2-}$ along the path $9 \rightarrow 0$. Refer to the caption of Fig. 2 and the text for further explanation.

$(2-) \rightarrow Si_{Si}\,(2-)$, the AIMD starting from the 9thNN showed that the recombination path was following an interstitialcy mechanism, the Si_{TC} (0) atom (Si1) kicked out another Si atom (Si2), and then the Si2 atom recombined with V_{Si} $(2-)$, as shown in Fig. 3(b). The recombination barrier is 1.85 eV, which is much higher than the barrier of $Si_{sp\langle 110\rangle} + V_{Si}$ $(2-) \rightarrow Si_{Si}$ $(2-)$. Since the barrier for the transformation of neutral Si_{TC} to $Si_{sp\langle 110\rangle}$ is about 0.5 eV from our calculation, the recombination for Si_{TC} will involve one more additional step where Si_{TC} transforms to $Si_{sp\langle 110\rangle}$, then $Si_{sp\langle 110\rangle}$ recombines with V_{Si}^{2-}. Thus, for the SiC with μ_F at conduction band minimum, the recombination of Si FP is also limited by the migration barrier of 0.80 eV for $Si_{sp\langle 110\rangle}$.

C. Kick-out reaction $C_i + Si_C \rightarrow C_C + Si_i$

This annealing reaction occurs by removing an antisite Si_C, which was considered as an important defect in the amorphization of SiC based on a recent *ab initio* rate theory model.[12] Antisites play an important role when the chemical disorder is thought to cause the amorphization in SiC, as proposed in Refs. 55–57. From the AIMD simulation with a starting point of 4thNN (neutral $C_i + Si_C$) for *n*-type SiC, the C_i atom started from position 4 ($C_{sp\langle 001\rangle tilted}$), passed position 1 ($C_{spSi\langle 010\rangle tilted}$), and kicked out the antisite Si_C atom (Si1) at position 0. Then Si1 formed a Si-split dumbbell interstitial ($Si_{sp\langle 110\rangle}$) with another Si atom (Si34), which is the 1stNN of the original Si_C. Thus the path from AIMD is $4 \rightarrow 1 \rightarrow 0$, as shown in Fig. 4(a). From the CI-NEB method, the barrier for the hop $4 \rightarrow 1$ is 0.61 eV, which is comparable to the migration barrier of $C_{sp\langle 100\rangle}$ (0.60 eV). When the C_i atom arrives at the 1stNN position, if it undergoes a forward hop $1 \rightarrow 0$, the barrier is 1.34 eV (E_r); however, if it goes backward for a hop $1 \rightarrow 4$, it needs to overcome a barrier of 1.67 eV (E_t). As both E_r and E_t are higher than the migration barrier of $C_{sp\langle 100\rangle}$ (0.60 eV), the EL for this reaction $C_{sp\langle 001\rangle}+Si_C \rightarrow C_C+Si_{sp\langle 110\rangle}$ is a trapping profile. Thus, it is possible that the C_i atom is trapped at the 1stNN. Such stable interstitial-antisite clusters have been observed in MD simulations,[58] and, in some cases, clusters have shown to be reasons for amorphization.[59] Considering the stability of the trapped state, we can regard the reaction $C_{sp\langle 001\rangle}+Si_C \rightarrow C_C+Si_{sp\langle 110\rangle}$ as two reactions (i) $C_{sp\langle 001\rangle}+Si_C \rightarrow C_{spSi\langle 010\rangle}-Si_C$ and (ii) $C_{spSi\langle 010\rangle}-Si_C \rightarrow C_C+Si_{sp\langle 110\rangle}$, where $C_{spSi\langle 010\rangle}-Si_C$ represents the trapped interstitial-antisite cluster. Reaction (i) has a forward barrier similar to the migration barrier of $C_{sp\langle 100\rangle}$ but has a relatively large backward barrier, which indicates that the cluster $C_{spSi\langle 010\rangle}-Si_C$ is hard to dissociate. Reaction (ii) shows $C_{spSi\langle 010\rangle}$ kicking out Si_C and has a barrier of 1.34 eV. As shown in Refs. 12 and 60, there was no significant influence on the critical temperature of amorphization associated with treating this reaction as one step or explicitly including the intermediate-trapped state and treating it as two reactions. We will generally use the reaction $C_i + Si_C \rightarrow C_C+Si_i$ as a shorthand for the two reactions (i) and (ii) (e.g., as done in Sec. IV.3) but will provide data for both steps of the reaction.

If we consider the reaction $C_i + Si_C \rightarrow C_C+Si_i$ from the defects starting as 6thNN, the path is $6 \rightarrow 1 \rightarrow 0$, as shown in Fig. 4(b). The hop $6 \rightarrow 1$ has a barrier of 0.60 eV, the barrier of the forward hop $1 \rightarrow 0$ is 1.34 eV, and the barrier of the backward hop $1 \rightarrow 6$ is 1.75 eV. Both paths $4 \rightarrow 1 \rightarrow 0$ and $6 \rightarrow 1 \rightarrow 0$ have essentially the same trapping profile and similar values of E_r and E_t. The reaction $C_{sp\langle 100\rangle}+Si_C \rightarrow C_C+Si_{sp\langle 110\rangle}$ along path $6 \rightarrow 1 \rightarrow 0$ is also equivalent to the two reactions (i) $C_{sp\langle 100\rangle}+Si_C C_{spSi\langle 010\rangle}-Si_C$ and (ii) $C_{spSi\langle 010\rangle}-Si_C \rightarrow C_C+Si_{sp\langle 110\rangle}$. Reaction (ii) is the rate-limiting reaction with a barrier of 1.34 eV obtained from CI-NEB. We find a barrier of 1.41 eV using the drag method, which is only 0.07 eV higher and suggests that the CI-NEB is robust.

When μ_F is around the midgap, the stable charge state of defect pair $C_{sp\langle 100\rangle}+Si_C$ is $2+$, which is contributed by the interstitial $C_{sp\langle 100\rangle}^{2+}$. When starting from the positions found for the neutral defect path, the kick-out reaction $C_{sp\langle 100\rangle}^{2+}+Si_C \rightarrow C_C+Si_{sp\langle 110\rangle}^{2+}$ changes little and remains similar to that of the neutral charge state. In this case, the rate limiting hop is also $1 \rightarrow 0$ (reaction $(C_{sp\langle 100\rangle}-Si_C)^{2+} \rightarrow C_C+Si_{sp\langle 110\rangle}^{2+}$), and the barrier is 2.24 eV, which is higher than both the

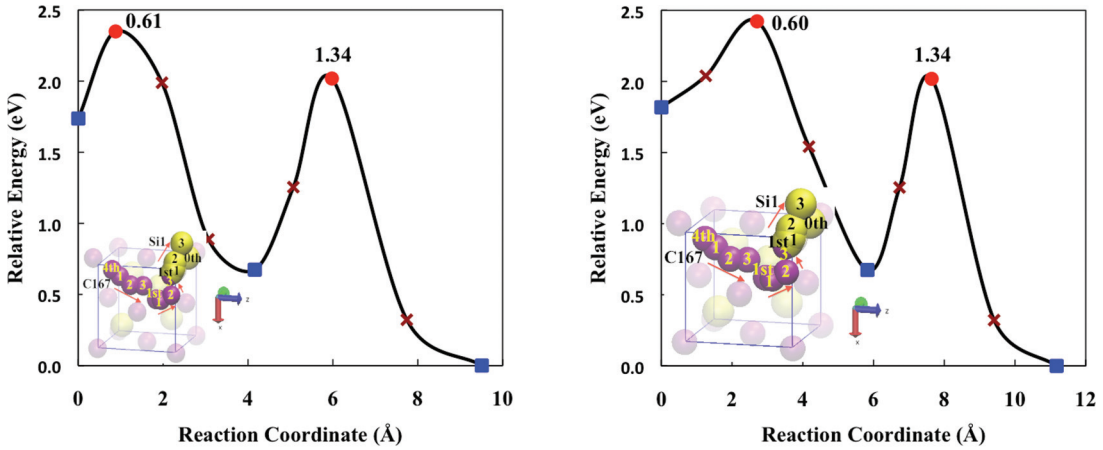

FIG. 4. (Color online) ELs of $C_i + Si_C \rightarrow C_C + Si_i$ along paths (a) $4 \rightarrow 1 \rightarrow 0$ and (b) $6 \rightarrow 1 \rightarrow 0$. The bright yellow balls are the Si_i atoms in the endpoints and images of CI-NEB. Refer to the caption of Fig. 2 for further explanation.

neutral barrier 1.34 eV and the migration barrier 1.40 eV for $C^{2+}_{sp\langle 100\rangle}$.[27]

D. Kick-out reaction $Si_i + C_{Si} \rightarrow Si_{Si} + C_i$

For the annealing between Si_i and C_{Si}, AIMD suggests two mechanisms for the path before the interstitial atom kicks out the antisite atom: (i) interstitialcy mechanism, where the Si-interstitial atom kicks out another Si atom; and (ii) interstitial (diffusing) mechanism, where the Si-interstitial atom diffuses by hops between interstitial sites. For the interstitialcy mechanism, the reaction path obtained from AIMD is along $4 \rightarrow 2/2' \rightarrow 0$, as shown by the insets of Fig. 5(a). At the initial point the 4thNN, Si1 and Si34 formed a Si-Si dumbbell ($Si_{sp\langle 1\bar{1}0\rangle}$) at the upper left corner. The interstitial atom Si1 starting from the 4thNN moved to kick out Si16 and replaced it at the front face center. Si16 became the moving interstitial atom and kicked out C217 at the upper right corner (0thNN). Finally, C217 formed a C-C dumbbell with C150 ($C_{sp\langle 001\rangle tilted}$). The barrier along this kicking out path $4 \rightarrow 2/2' \rightarrow 0$ is 0.97 eV, whose EL has a recombination profile, as shown in Fig. 5(a).

If the Si_i atom (Si1) followed the diffusing path, it moved along $4 \rightarrow 0$ to kick out the antisite C_{Si} atom (C217), as shown by the insets of Fig. 5(b). Si1 moved along a tilted $\langle 001\rangle$ direction passing the 3rdNN ($Si_{spC\langle 010\rangle tilted}$). Then Si1 kicked out C217, which formed a C-split dumbbell interstitial ($C_{sp\langle 001\rangle tilted}$) with C150 at the nearest interstitial site of the original antisite. The energy barrier along the path $4 \rightarrow 0$ is 0.64 eV from CI-NEB (0.67 eV from the drag method). This energy barrier of the diffusing path is lower than that of the above interstitialcy path. Thus, the migration path $4 \rightarrow 0$ is preferred. Therefore, the final energy barrier of this kick-out reaction is 0.64 eV, which is lower than the migration

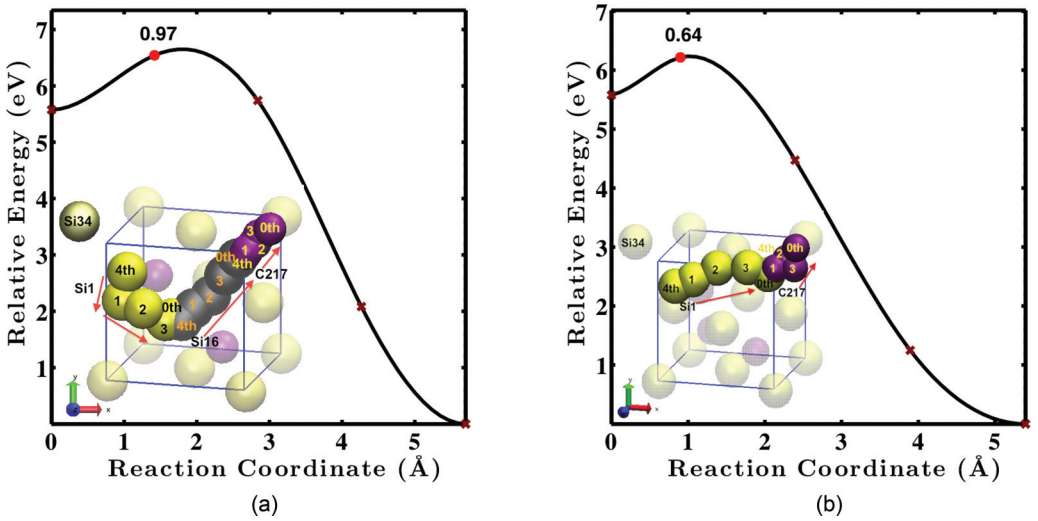

FIG. 5. (Color online) ELs of $Si_i + C_{Si} \rightarrow Si_{Si} + C_i$ along paths (a) $4 \rightarrow 2/2' \rightarrow 0$ and (b) $4 \rightarrow 0$. From the inset of (a), at the initial point (4thNN), Si1 and Si34 form a Si-Si dumbbell. Then Si1 (bright yellow ball) kicks out Si16 (gray ball), and Si16 kicks out C217 (dark purple ball). The inset of (b) shows that Si1 (bright yellow ball) diffuses along the path $4 \rightarrow 0$ and kicks out C217 (dark purple ball) at the 0thNN. Refer to the caption of Fig. 2 for further explanation.

barrier of $Si_{sp\langle 110\rangle}$ (0.80 eV). Thus, the EL of this reaction $Si_{sp\langle 110\rangle}+C_{Si} \rightarrow Si_{Si}+C_{sp\langle 100\rangle}$ is a migration profile, as shown in Fig. 5(b).

When μ_F is around the midgap, the stable charge state of the defect pair $Si_{sp\langle 110\rangle}+C_{Si}$ is $2+$, which is mainly contributed from $Si^{2+}_{sp\langle 110\rangle}$. For the kick-out reaction of charged defects $Si^{2+}_{sp\langle 110\rangle}+C_{Si} \rightarrow Si_{Si}+C^{2+}_{sp\langle 100\rangle}$, we took the neutral defect recombination path $4 \rightarrow 0$ as the initial path for the CI-NEB run. After calculation, a similar recombination path as the neutral case and lower barrier of 0.35 eV was obtained.

V. DISCUSSION

We now compare our results on the recombination barriers calculated using *ab initio* works with those from previous calculations and experiments. We note that for the cases tested, the barriers for the same mechanism calculated in a similar manner but with different DFT exchange-correlation approaches are generally relatively close to each other. The barrier difference between the available GGA/LDA/GW/hybrid calculations seems to be about 0.2 eV or less. All differences in GGA and LDA values (a total of 10 tests done in this work) in Table IV are 0.21 eV or less except for one value of 0.27 eV, which corresponds to a barrier of about 6 eV and is therefore still a very small percentage error. There are to date limited GW- and hybrid-barrier studies, so one cannot reliably know the impact of these more accurate methods on the migration kinetics. However, in Ref. 24, the barrier of transformation $V^{-}_{Si} \rightarrow (V_C + C_{Si})^{-}$ calculated using GW is only 0.15 eV (∼6%) lower than that from LDA with the same charge state. In Ref. 61, the migration barrier for oxygen interstitial in silicon from GGA is 0.32 eV (∼12%) lower than that from a hybrid calculation. In practice, if the deviation of barriers between our work and others is larger than 0.2 eV (∼15%), it is typically due to having found different pathways or other reasons besides the DFT exchange-correlation approaches.

For the neutral recombination reaction $C_i + V_C \rightarrow C_C$ (μ_F at conduction band minimum), we found a curved recombining path $4 \rightarrow 2 \rightarrow 1 \rightarrow 0$ with a recombination barrier of 0.90 eV. In Ref. 29, the recombination barrier was found to be 1.35 eV. It appears from Ref. 29 that the barrier was calculated along a different path, which was a combination of NEB paths ($4 \rightarrow 2$, $1 \rightarrow 0$) and a constrained relaxation path ($2 \rightarrow 0$). This difference in path is a likely explanation for why we found a different energy barrier. In Ref. 31, the barrier was 1.47 eV along a straight path $4 \rightarrow 0$ in the ⟨100⟩ direction. Their CI-NEB images were obtained through the linear interpolation. We also checked this straight path $4 \rightarrow 0$ and found its barrier (1.48 eV) was higher than that along the curved path $4 \rightarrow 2 \rightarrow 1 \rightarrow 0$ (0.90 eV) we found. Our barrier for the recombination of close C FP (hop $2 \rightarrow 0$) is 0.43 eV for the neutral state and 0.49 eV for the charge $1+$ state, which are close to the 0.4 eV (neutral) and 0.5 eV ($1+$) in Ref. 30. These values agree fairly well with the barriers (0.24 ∼ 0.38 eV) proposed from the MD simulation for close FP recombination in Ref. 22. However, for C FP where the participating defects are well separated (the distance between C_i and V_C $d_{def} > 0.7a_0$), the long-range interaction between C_i and V_C make the kinetics significantly different from that of free-interstitial diffusion.

Our results of the recombination barriers of neutral Si FP agree with the data in the literature. For example, our barrier of $Si_{sp\langle 110\rangle} + V_{Si} \rightarrow Si_{Si}$ along the path $6 \rightarrow 2/2' \rightarrow 0$ is 0.03 eV, which is the same as the corresponding barrier in Ref. 29. For neutral reaction $Si_{TC} + V_{Si} \rightarrow Si_{Si}$, we obtained barriers for hops $3 \rightarrow 0$ (interstitialcy) and $9 \rightarrow 0$ (interstitialcy) as 2.26 eV and 1.76 eV, corresponding to the barriers in Ref. 31 of 2.37 eV and 1.84 eV, respectively. Furthermore, we determine the final recombination path barrier for Si FP recombination when μ_F is at both midgap and conduction band minimum.

For the kick-out reaction $C_i + Si_C \rightarrow C_C + Si_i$, we find a trapping path $4 \rightarrow 1 \rightarrow 0$ with a forward barrier 1.34 eV and a backward barrier 1.67 eV. A trapping profile was also found by Bockstedte *et al.*[30] with a 2-eV forward barrier and a 3-eV backward barrier, but no explicit path was shown. The stable-trapped interstitial and antisite cluster has also been observed in MD simulations with interatomic potentials.[58] Finally, there has been no previous work of which we are aware on the kick-out reaction $Si_i + C_{Si} \rightarrow Si_{Si} + C_i$.

Based on our analysis, we conclude that the differences in computed barriers reported in the literature for apparently similar reactions are mainly due to the different migration paths that are considered in those studies. Compared to the previous computational results, we have found paths with either a similar or lower energy barriers for each point-defect reaction in both neutral and charge states. Here, we summarize the results in Table V and compare them to inferred barriers from isochronal annealing experiments which associate specific barriers to defect recovery stages.

(1) C FP recombination $C_i + V_C \rightarrow C_C$ occurs along a recombining path $4 \rightarrow 2 \rightarrow 1 \rightarrow 0$ with a barrier of 0.90 eV for neutral state when μ_F is at the conduction band minimum and 1.88 eV for $4+$ charge state when μ_F at midgap. The 0.90-eV barrier is close to the activation energies of stage II 0.7 ± 0.2 eV from D^+ channeling analysis[32] and 0.89 ± 0.02 eV from the RBS and thermal annealing experiments.[23,33] The barrier of closer C FP (hop $2 \rightarrow 0$) is 0.43 eV; thus, the recombination barrier of closer C FPs is limited by the migration barrier of $C_{sp\langle 100\rangle}$ (0.60 eV) and is likely related to the activation energy of 0.49 eV for recovery stage I (assessed from DLTS and resistivity measurements[16]). The large barrier of 1.88 eV for $4+$-charge state when μ_F at midgap is close to the energy barrier value 2.20 ± 0.30 eV (see Ref. 18) in the recovery stage III. These results show that the close C-FP recombination is consistent with the activation energy of recovery stage I, the well-separated neutral C-FP recombination is associated with the activation energy of recovery stage II, and the charged C-FP ($4+$) recombination is related to the activation energy of recovery stage III.

(2) Si FP recombination, including $Si_{sp\langle 110\rangle} + V_{Si} \rightarrow Si_{Si}$ and $Si_{TC} + V_{Si} \rightarrow Si_{Si}$, is rate-limited by $Si_{sp\langle 110\rangle} + V_{Si} \rightarrow Si_{Si}$. This reaction happens along an interstitialcy path $6 \rightarrow 2/2' \rightarrow 0$, the barrier is 0.03 eV for neutral $Si_{sp\langle 110\rangle} + V_{Si}$ with μ_F at midgap and is 0.17 eV for the charged $Si_{sp\langle 110\rangle} + V_{Si}$ ($2-$) with μ_F at the conduction band minimum. The motion of $Si_{sp\langle 110\rangle}$ is limited by its migration barrier 0.80 eV. Thus, the migration and recombination of $Si_{sp\langle 110\rangle}$ is governed by a barrier of 0.80 eV and consistent with the recovery stage II.

TABLE V. Summary of the energy barriers (E_r) of point-defect reactions compared with the corresponding migration barriers (E_m) of mobile defects in SiC and possible associated recovery stages whose activation energy is determined by max(E_r, E_m).

Reactions	$C_{sp\langle 100\rangle} + V_C \rightarrow C_C$		$Si_{sp\langle 110\rangle} + V_{Si} \rightarrow Si_{Si}$	$C_i + Si_C \rightarrow C_C + Si_i$		$Si_i + C_{Si} \rightarrow Si_{Si} + C_i$
Path (charge)	$2 \rightarrow 0$ (0)	$4 \rightarrow 2 \rightarrow 1 \rightarrow 0$ (0/4+)	$6 \rightarrow 2/2' \rightarrow 0$ (0/2−)	$C_i + Si_C \rightarrow C_i - Si_C$ (0)	$C_i - SiC \rightarrow C_C + Si_i$ (0/2+)	$4 \rightarrow 0$ (0/2+)
EL type	Migration	Recombination	Migration	Trapping		Migration
E_r (eV)	0.43	0.90/1.88	0.03/0.17	0.61	1.34/2.24	0.64/0.35
E_m (eV)	0.60	0.60	0.83	0.60	0.60	0.83
Stage I	Y			Y		
Stage II		Y	Y			Y
Stage III		Y			Y	

(3) C interstitial and Si antisite kick-out reaction $C_i + Si_C \rightarrow C_C + Si_i$ happens along a trapping path $4 \rightarrow 1 \rightarrow 0$ with a barrier of 1.34 eV for neutral state (μ_F at conduction band minimum) and 2.24 eV for charge 2+ state (μ_F at midgap). The neutral state barrier matches with the experimental activation energies of recovery stage III 1.50 ± 0.30 eV in Ref. 2 and 1.30 ± 0.20 eV in Ref. 32, and the 2+ charge state value 2.24 eV is similar to the experimental energy 2.20 ± 0.30 eV in Ref. 18, which was also associated with the recovery stage III. It has not previously been clear that mechanism might explain the high barriers observed in stage III annealing. Reference 24 assigned the rate-limiting mechanism to the transformation $V_{Si} \rightarrow V_C + C_{Si}$, which was calculated to have a barrier of 2.32 eV. However, this reaction does not provide a clear path to healing, either through annihilating defects completely or by transforming defects into something with enough mobility to annihilate at the relevant temperatures. In Ref. 23, the migration barrier of V_{Si} was calculated to be 2.35 eV, but since the migration barrier of $Si_{sp\langle 110\rangle}$ is much lower, it might be expected that the Si recombination happens at lower temperature by the migration of Si_i rather than V_{Si}. However, since the mobile Si_i can annihilate with not only V_{Si} but also other defects or sinks, V_{Si} may be left over and be healed during stage III. The migration energy of V_{Si} is somewhat too high for most of the stage III energies that have been identified but is consistent with the highest values of stage III energies that have been measured.[18] Furthermore, it is reasonable to assume that the stage III healing processes are those that control amorphization, but the migration energy of V_{Si} is too high a value to be consistent with controlling amorphization temperatures [300 ∼ 500 K in SiC, consistent with ∼1.4 eV (see Ref. 60)]. Therefore, it is not clear how significant a role, if any, is played by V_{Si} mobility in the annealing stages of any given irradiated SiC. We propose that this stage III is dominated by the $C_i + Si_C \rightarrow C_C + Si_i$ reaction. Note that the Si_i yielded by the reaction $C_i + Si_C \rightarrow C_C + Si_i$ is mobile and can easily recombine with V_{Si} at stage III temperatures. Therefore, when combined with Si FP recombination, this kick-out reaction potentially allows for removal of all the defects involved in both reactions. Thus, the annealing between C_i and Si_C through this kick-out reaction could be the process associated with the recovery stage III. We also note that this reaction provides an energy barrier close to that associated with the critical temperature range to amorphization (300 ∼ 500 K) in SiC [consistent with energy barriers ∼1.4 eV (see Ref. 60. Recent rate theory modeling[12] suggested that this C_i and Si_C kick-out reaction could play the key role in setting SiC's critical temperature to amorphization.

We also note that to reverse this reaction, the total barrier is 2.02 eV (2.02 eV to return to the bound $C_i + Si_C$ complex and then 1.67 eV to unbind), which provides a possible mechanism to transform Si_i into C_i. Even though this reverse reaction happens, healing mechanisms for Si_i point-defect types are predicted to be active at even lower temperatures, so we do not expect this transformation will have any particular impact on defect healing.

(4) Si interstitial and C antisite kick-out $Si_i + C_{Si} \rightarrow Si_{Si} + C_i$ takes place along a migration path $4 \rightarrow 0$ with a barrier of 0.64 eV for neutral state (μ_F at conduction band minimum) and 0.35 eV for charge 2+ state (μ_F at midgap). Thus, this reaction is kinetically limited by the migration barrier of $Si_{sp\langle 110\rangle}$, which is 0.80 eV. This energy barrier is in the range of the experimental activation energies of stage II, which are 0.7 ± 0.2 eV (see Ref. 32 and 0.9 eV (see Ref. 22). The annealing between Si_i and C_{Si} provides another possible mechanism active in the recovery stage II.

Based on the above discussion, we can make the following qualitative assignments for the active migration and recombination mechanisms involving binary defect reactions for each recovery stage. Stage I ($0.2\ \text{eV} < E_a < 0.5\ \text{eV}$) is associated with the migration of C_i and recombination of close C FP. Stage II ($0.7\ \text{eV} < E_a < 0.9\ \text{eV}$) is related to the well-separated C-FP recombination, or Si-FP recombination and Si_i and C_{Si} kick-out reaction, which are limited by the migration of $Si_{sp\langle 110\rangle}$. Stage III ($1.3\ \text{eV} < E_a < 2.4\ \text{eV}$) is attributed to the C_i and Si_C kick-out reaction with neutral state and charge 2+ state. Overall, if recovery stages I and II allow for the healing of all C interstitials, vacancies, and antisites [following the mechanisms described in items (1) and (4)], then the kick-out reactions combined with Si-FP recombination in stage III will allow for the healing of all the remaining damage in the material.

We note that these assignments for recovery stages in the thermal annealing process are based on the energetics of dilute defects. Such an approach is approximate, as the damaged material can have high defect concentrations, and defect interactions could significantly alter the dilute energetics. This defect interaction effect will be of particular concern for ion-irradiated materials, where the cascades may produce

many defect clusters with strongly interacting defects. We note that these approximations are therefore likely most accurate for mildly damaged materials with low defect concentrations and particularly for electron irradiated materials where the defects are, at least when formed, expected to be predominantly point defects not in clusters. It is interesting to note that for systems just above the amorphization temperature or in the ending portion of the near complete damage recovery during stage III, one expects relatively few defects. Provided these defects have not clustered, the dilute point-defect energetics calculated here would be expected to provide accurate energetics. Thus, for the critical properties of the amorphization temperature and the temperature of the final recovery stage (stage III), we expect the energies found in this work to suffer the least from the diluteness approximation. It is for exactly these key temperatures that the newly determined C_i and Si_C kick-out reaction barrier is predicted to play a dominant role.

VI. CONCLUSIONS

We have searched SiC point-defect recombination/kick-out paths by using AIMD simulations, CI-NEB, and drag methods. Applying these approaches, we find the minimum energy reaction paths and determine energy barriers of four key point-defect annealing reactions in neutral and correct charge states for both midgap and n-type SiC. Our results generally agree with previous calculations for similar paths, help resolve some apparent discrepancies in the literature, and in a number of cases provide lower activation energy pathways than previously identified. Our barriers are consistent with those estimated from recovery experiments and provide a possible mapping of the basic binary defect reactions onto the SiC recovery stages. In particular, our barriers suggest that the C interstitial and Si antisite kick-out reaction $C_i + Si_C \rightarrow C_C + Si_i$ is a critical mechanism for the recovery stage III and may set the critical temperature to amorphization in SiC.

ACKNOWLEDGMENTS

NS, DM, and IS gratefully acknowledge support from the U.S. Department of Energy, Office of Basic Energy Sciences under Grant No. DE-FG02-08ER46493. M-JZ was supported by the funding from the DOE Office of Nuclear Energy's Nuclear Energy University Programs (NEUP 10-679). This work benefitted from the use of the Extreme Science and Engineering Discovery Environment (XSEDE), which is supported by National Science Foundation grant number OCI-1053575.

*ddmorgan@wisc.edu
†szlufarska@wisc.edu

[1] P. Fenici, A. J. Frias Rebelo, R. H. Jones, A. Kohyama, and L. L. Snead, J. Nucl. Mater. **258-263 Part 1**, 215 (1998).
[2] W. J. Weber, W. Jiang, and S. Thevuthasan, Nucl. Instrum. Methods Phys. Res., Sect. B **175-177**, 26 (2001).
[3] S. J. Zinkle and J. T. Busby, Materials Today **12**, 12 (2009).
[4] E. Lopez-Honorato, J. Tan, P. J. Meadows, G. Marsh, and P. Xiao, J. Nucl. Mater. **392**, 219 (2009).
[5] Y. Katoh, L. L. Snead, I. Szlufarska, and W. J. Weber, Curr. Opin. Solid State Mater. Sci. **16**, 143 (2012).
[6] V. I. Ivashchenko, P. E. A. Turchi, and V. I. Shevchenko, Phys. Rev. B **75**, 085209 (2007).
[7] M. Ishimaru, I.-T. Bae, A. Hirata, Y. Hirotsu, J. A. Valdez, and K. E. Sickafus, Phys. Rev. B **72**, 024116 (2005).
[8] W. J. Weber, L. M. Wang, N. Yu, and N. J. Hess, Mater. Sci. Eng. A **253**, 62 (1998).
[9] R. H. Jones, L. Giancarli, A. Hasegawa, Y. Katoh, A. Kohyama, B. Riccardi, L. L. Snead, and W. J. Weber, J. Nucl. Mater. **307-311, Part 2**, 1057 (2002).
[10] A. T. Motta, J. Nucl. Mater. **244**, 227 (1997).
[11] H. Inui, H. Mori, A. Suzuki, and H. Fujita, Philos. Mag. B **65**, 1 (1992).
[12] N. Swaminathan, D. Morgan, and I. Szlufarska, J. Nucl. Mater. **414**, 431 (2011).
[13] J. J. A. Freitas, S. G. Bishop, J. A. Edmond, J. Ryu, and R. F. Davis, J. Appl. Phys. **61**, 2011 (1987).
[14] N. T. Son, E. Sorman, W. M. Chen, M. Singh, C. Hallin, O. Kordina, B. Monemar, E. Janzen, and J. L. Lindstrom, J. Appl. Phys. **79**, 3784 (1996).
[15] A. Kawasuso, F. Redmann, R. Krause-Rehberg, T. Frank, M. Weidner, G. Pensl, P. Sperr, and H. Itoh, J. Appl. Phys. **90**, 3377 (2001).
[16] V. Nagesh, J. W. Farmer, R. F. Davis, and H. S. Kong, Appl. Phys. Lett. **50**, 1138 (1987).
[17] H. Itoh, A. Kawasuso, T. Ohshima, M. Yoshikawa, I. Nashiyama, S. Tanigawa, S. Misawa, H. Okumura, and S. Yoshida, Phys. Status Solidi A **162**, 173 (1997).
[18] H. Itoh, N. Hayakawa, I. Nashiyama, and E. Sakuma, J. Appl. Phys. **66**, 4529 (1989).
[19] W. J. Weber, W. Jiang, and S. Thevuthasan, Nucl. Instrum. Methods Phys. Res., Sect. B **166-167**, 410 (2000).
[20] G. Alfieri, E. V. Monakhov, B. G. Svensson, and M. K. Linnarsson, J. Appl. Phys. **98**, 043518 (2005).
[21] K. Danno and T. Kimoto, J. Appl. Phys. **101**, 103704 (2007).
[22] F. Gao and W. J. Weber, J. Appl. Phys. **94**, 4348 (2003).
[23] F. Gao, W. J. Weber, M. Posselt, and V. Belko, Phys. Rev. B **69**, 245205 (2004).
[24] F. Bruneval and G. Roma, Phys. Rev. B **83**, 144116 (2011).
[25] S. Kondo, Y. Katoh, and L. L. Snead, Phys. Rev. B **83**, 075202 (2011).
[26] D. Shrader, S. M. Khalil, T. Gerczak, T. R. Allen, A. J. Heim, I. Szlufarska, and D. Morgan, J. Nucl. Mater. **408**, 257 (2011).
[27] M. Bockstedte, A. Mattausch, and O. Pankratov, Phys. Rev. B **68**, 205201 (2003).
[28] Z. Rong, F. Gao, W. J. Weber, and G. Hobler, J. Appl. Phys. **102**, 103508 (2007).
[29] G. Roma and J. P. Crocombette, J. Nucl. Mater. **403**, 32 (2010).
[30] M. Bockstedte, A. Mattausch, and O. Pankratov, Phys. Rev. B **69**, 235202 (2004).
[31] G. Lucas and L. Pizzagalli, J. Phys.: Condens. Matter **19**, 086208 (2007).
[32] W. Jiang, Y. Zhang, and W. J. Weber, Phys. Rev. B **70**, 165208 (2004).
[33] Y. Zhang, W. J. Weber, W. Jiang, A. Hallen, and G. Possnert, J. Appl. Phys. **91**, 6388 (2002).

[34]G. Henkelman, B. P. Uberuaga, and H. Jonsson, J. Chem. Phys. **113**, 9901 (2000).
[35]M. Bockstedte and M. Scheffler, Z. Phys. Chemie-Int. J. Res. Phys. Chem. Chem. Phys. **200**, 195 (1997).
[36]G. Kresse and J. Furthmuller, Comput. Mater. Sci. **6**, 15 (1996).
[37]G. Kresse and J. Furthmuller, Phys. Rev. B **54**, 11169 (1996).
[38]G. Kresse and J. Hafner, Phys. Rev. B **47**, 558 (1993).
[39]G. Kresse and J. Hafner, Phys. Rev. B **49**, 14251 (1994).
[40]J. P. Perdew, K. Burke, and M. Ernzerhof, Phys. Rev. Lett. **77**, 3865 (1996).
[41]E. Rauls, T. Frauenheim, A. Gali, and P. Deak, Phys. Rev. B **68**, 155208 (2003).
[42]G. Makov and M. C. Payne, Phys. Rev. B **51**, 4014 (1995).
[43]M. Leslie and N. J. Gillan, J. Phys. C **18**, 973 (1985).
[44]H. J. Kim and R. F. Davis, J. Electrochem. Soc. **133**, 2350 (1986).
[45]J. B. Casady and R. W. Johnson, Solid State Electron. **39**, 1409 (1996).
[46]C. Wang, J. Bernholc, and R. F. Davis, Phys. Rev. B **38**, 12752 (1988).
[47]T. Tachibana, H. S. Kong, Y. C. Wang, and R. F. Davis, J. Appl. Phys. **67**, 6375 (1990).
[48]W. J. Choyke, H. Matsunami, and G. Pensl (eds.), *Silicon Carbide Recent Major Advances* (Springer, Berlin, 2004).
[49]M. E. Levinshtein, S. L. Rumyantsev, and M. S. Shur, *Properties of Advanced Semiconductor Materials: GaN, AlN, InN, BN, SiC, and SiGe* (Wiley, New York, 2001).
[50]G. A. Baraff and M. Schlüter, Phys. Rev. B **30**, 1853 (1984).
[51]P. Deak, T. Frauenheim, and A. Gali, Phys. Rev. B **75**, 153204 (2007).
[52]F. Bruneval, Nucl. Instrum. Methods Phys. Res., Sect. B **277**, 77 (2012).
[53]T. Oda, Y. Zhang, and W. J. Weber, Chem. Phys. Lett. **579**, 58 (2013).
[54]R. Devanathan, W. J. Weber, and F. Gao, J. Appl. Phys. **90**, 2303 (2001).
[55]L. W. Hobbs, A. N. Sreeram, C. E. Jesurum, and B. A. Berger, Nucl. Instrum. Methods Phys. Res., Sect. B **116**, 18 (1996).
[56]F. Gao and W. J. Weber, J. Appl. Phys. **89**, 4275 (2001).
[57]X. Yuan and L. W. Hobbs, Nucl. Instrum. Methods Phys. Res., Sect. B **191**, 74 (2002).
[58]W. J. Weber and F. Gao, J. Mater. Res. **25**, 2349 (2010).
[59]D. F. Pedraza, J. Mater. Res. **1**, 425 (1986).
[60]N. Swaminathan, D. Morgan, and I. Szlufarska, Phys. Rev. B **86**, 214110 (2012).
[61]P. Deák, A. Gali, B. Aradi, and T. Frauenheim, Phys. Status Solidi B **248**, 790 (2011).